ORNL/SPR-2021/2122

Development and Implementation of Digital Image Correlation for Out-of-Cell Burst Testing

Nuclear Technology Research and Development

Prepared for
U.S. Department of Energy
Nuclear Technology R&D Program
Advanced Fuels Campaign

Kenneth Kane[1], Nathan Capps,[1] Ben Garrison[1], Brandon Johnston[1], Samuel Bell,[2] Kory Linton[1]
[1]Oak Ridge National Laboratory
[2]University of Tennessee, Knoxville

August 2021
M3FT-21OR020204075

DISCLAIMER

This information was prepared as an account of work sponsored by an agency of the U.S. Government. Neither the U.S. Government nor any agency thereof, nor any of their employees, makes any warranty, expressed or implied, or assumes any legal liability or responsibility for the accuracy, completeness, or usefulness, of any information, apparatus, product, or process disclosed, or represents that its use would not infringe privately owned rights. References herein to any specific commercial product, process, or service by trade name, trade mark, manufacturer, or otherwise, does not necessarily constitute or imply its endorsement, recommendation, or favoring by the U.S. Government or any agency thereof. The views and opinions of authors expressed herein do not necessarily state or reflect those of the U.S. Government or any agency thereof.

ACKNOWLEDGEMENTS

This work was supported by the Advanced Fuels Campaign of the US Department of Energy Office of Nuclear Energy. The authors would like to express appreciation to Jason Harp and Caleb Massey (Oak Ridge National Laboratory) for their technical review, and to Laurent Capolungo (Los Alamos National Laboratory) for providing technical guidance.

SUMMARY

This report details the progress made towards utilizing *in-situ* methods to observe and quantify unirradiated Zircaloy-4 (Zr4) fuel cladding deformation during out-of-cell design basis accident conditions, specifically during loss-of-coolant accident (LOCA) burst testing in the Severe Accident Test Station at Oak Ridge National Laboratory. Digital image correlation (DIC) was implemented to calculate cladding strain during burst and infrared (IR) thermography was used to attempt a correlation of strain with temperature and to investigate thermal gradients. For both techniques, early experimentation revealed experimental modifications were necessary for implementation. For DIC, this manifested as shortened cladding lengths which could be centered in front of the viewing chamber bored through the IR furnace side, and for IR thermography this meant conducting burst tests in air without a reaction tube and the incorporation of a SiC shell to eliminate direct IR reflections from the tungsten lamps. In the following, the technical issues and subsequent origin of these modifications are discussed, laying the framework for a proof-of-concept DIC/IR characterization of a burst test in the final section.

CONTENTS

ACKNOWLEDGEMENTS iii

SUMMARY iv

FIGURES vi

ACRONYMS viii

1. Introduction 1

2. Summary of Experimental Design 2

3. Infrared Thermography 3
   - 3.1 Planck's Law 3
   - 3.2 Emissivity and IR Reflectivity 5
   - 3.3 IR Reflectivity During Burst Testing 7
   - 3.4 Implementation of SiC "C' Shell to eliminate IR reflectivity 9

4. Digital Image Correlation 13

5. In-Situ Observation of Cladding Deformation during Burst 16
   - 5.1 Experimental details 16
   - 5.2 Burst Test at Nominal Initial 8.2 MPa Overpressure 17
     - 5.2.1 Temperature/Pressure Profile and Burst Hoop Stress 17
     - 5.2.2 Optical Observation of Cladding Deformation 20
     - 5.2.3 Correlation of DIC Strain with IR Imaging 22

6. Summary and Conclusions 23

7. References 24

FIGURES

Figure 2-1 Experimental set up with primary components labelled. Over the course of experimentation, some primary components are removed from the set up and will be denoted accordingly. 3

Figure 3-1 Visible and infrared electromagnetic spectrum 4

Figure 3-2 Spectral energy density (Planck's Law) of a blackbody's emission as a function of wavelength and temperature. 5

Figure 3-3 Response of a (a) blackbody and (b) graybody object to incident IR radiation from a W-filament IR lamp 6

Figure 3-4 Schematic showing the differences in the IR furnaces used (a) previously for standard LOCA burst testing and (b) presently for observing in-situ cladding deformation during LOCA like conditions. 7

Figure 3-5 (a) IR thermal map and (b) optical image of pressurized Zr4 cladding during 5°C/s heating prior to visible deformation and (c) IR thermal map and (d) optical image of cladding immediately prior to burst. 8

Figure 3-6 (a) Conceptual illustration of a SiC "C" shell blocking direct IR radiation of cladding during burst testing. (b) Macrograph of cladding train assembly utilizing 76 mm Zr4 cladding length and SiC "C" shell. (c) Optical image showing assembly sitting in furnace through the viewing chamber. 10

Figure 3-7 (a) Macrograph showing IR camera point-of-view when positioned directly in front of the viewing chamber and (b) associated IR image of un-pressurized Zr4 cladding when T_{Sample} = 757°C. (c) Macrograph showing IR camera point-of-view when observing viewing chamber with IR mirror and (d) associated IR image, also when T_{Sample} = 757°C. 11

Figure 3-8 (a) Visible light transmission coefficient and IR light reflection coefficient of the IR mirror. The mirror specifications are highlighted by grey shaded boxes, while the experimentally determined reflection coefficient over the 500° to 800°C range is shown by blue squares. On the RHS axis, the relationship between maximum wavelength emittance and temperature of a black body is shown (Wien's displacement law). (b) Necessary emissivity to match direct line-of-sight IR camera temperature to cladding temperature (T_{Sample}) determined with a thermocouple. 13

Figure 4-1 (a) Reference DIC image and (b)-(c) a series of optical images taken during 300° to 1200° temperature ramping. Estimated temperatures, determined from the thermocouple in the top regions of each image, are overlaid. 14

Figure 4-2 The DIC field placement (a) the reference image (image # 715) showing the node of interest and (b) image 885 showing loss of tracking for several nodes. 15

Figure 5-1 (a) Temperature and pressure profile during burst testing of 76 mm length Zr4 cladding in air with a 1°C/s heating rate. (b) Close up of profile when burst occurred. 18

Figure 5-2 Relationship between burst hoop stress and burst temperature of Zr4 cladding with vary lengths and heating rates. 19

Figure 5-3 (a) Diametrical strain along cladding length of (b) 76 mm and (c) 305 mm length Zr claddings burst at similar temperatures but with differing heating rates and gas environment. 20

Figure 5-4 (a) Optical image of laser engraved Zr4 cladding prior to significant ballooning during 300° to 1200°C ramp at 1°C/s taken at 1196 s and series of images spaced ~2 seconds apart leading to (b) cladding burst ~48 s later. 21

Figure 5-5 (a) Optical image showing colored strain map of hoop strain, immediately prior to burst. (b) Plot of the hoop, axial, and radial strain and internal pressure relationship with temperature, where hoop and axial strain was calculated over the entire 300° to 1200°C ramp (until burst) from the DIC object indicated in (a). Radial strain was calculated assuming conservation of volume based on the DIC-calculated hoop and axial strains, and its negative values suggest wall thinning, which is expected. 22

Figure 5-6 (a) Optical image of Zr4 cladding immediately prior to burst and (b) associated IR thermal image. (c) Line scan of thermal gradient down the cladding length, where direction and position are indicated by the white arrow in (b) and blue arrow in (c). 23

ACRONYMS

Loss-of-coolant accident	(LOCA)
Zircaloy-4	(Zr4)
Severe Accident Test Station	(SATS)
Oak Ridge National Laboratory	(ORNL)
Digital image correlation	(DIC)
Infrared	(IR)
Silicon carbide	(SiC)

DEVELOPMENT AND IMPLEMENTATION OF DIGITAL IMAGE CORRELATION FOR OUT-OF-CELL BURST TESTING

1. Introduction

Historically, Zircaloy ballooning and rupture testing during simulated loss-of-coolant accident (LOCA) testing utilized pre-pressurized ~300 mm length claddings and specified heating rates. Internal pressure and cladding temperature were measured via a single pressure transducer and thermocouple as a function of time, where rupture was marked by an abrupt drop in pressure. Quantifying cladding deformation rested primarily upon before and after comparisons, with no in-situ cladding deformation data to support concurrent model development or code validation. This procedure was used by multiple test programs, and the data generated from these programs were used to develop a heating rate-dependent (°C/s), stress-based burst criterion [1], shown in Eq. (1)

$$T_R = 3960 - \frac{20.4\sigma}{1+H} - \frac{8{,}510{,}000\sigma}{100(1+H)+27}, \qquad (1)$$

where T_R is the rupture temperature in degrees Celsius, σ is the engineering hoop stress in kpsi, and H is a ratio of the heating rate defined by Eq. (2):

$$H = \frac{x}{28}, \qquad (2)$$

where x is the heating rate during the LOCA event in °C/s. This criterion is inherently a nodal, 1-dimensional model, but cladding ballooning and rupture is a geometrically complex phenomenon. During experimentally simulated LOCA, cladding deformation behavior is biaxial with anisotropic behavior below 800°-850°C. Furthermore, the consequences of long periods of exposure to hydrothermal and irradiation conditions, like oxidation, hydrogen pick up, and irradiation hardening, aren't incorporated into the criteria.

To broaden the 1-D criteria, licensed fuel performance codes use spatial simplifications by assessing fuel conditions across a single axial plane or a series of axial planes [2], [3]. Provided that actual deformation is uniform or can be distilled into 1-D components, validating the performance codes is straightforward. However, Erbacher et al. [4]–[6] have highlighted that azimuthal temperature gradients can have a significant impact on cladding burst temperatures and stresses. Furthermore, recent cladding burst evaluations have confirmed that severe axial temperature gradients can also be present [7]–[9]. Still, there's little information regarding thermal gradients in areas ~5 mm away from burst, so no conclusions about deformation behavior can be made in these regions. Presumably, temperature continues to decrease further away from burst.

Recent work on FeCrAl cladding demonstrated that burst tests could be performed on 100 mm length segments instead of 250–300 mm lengths and generate similar burst conditions (e.g., temperature, balloon geometry, burst opening) [9]. If similar agreement between shorter and longer segment burst behavior exists for Zircaloy, the results suggest that cladding burst depends on the local effects and not the cladding specimen length, and furthermore that any modeling approach that interpolates across axial planes will fail to capture the full effect of the various fuel irradiation processes (e.g., volumetric change, plenum pressure

evolution, axial and azimuthal temperature variations, etc.) associated with LOCA progression. More advanced 1-D and 2-D modelling have to impose a cosine-shaped axial heating profile to ensure burst occurs at a specified region. However, this assumption tends to be on the order of ~ 50°C over ~15 cm, whereas recent experimental data shows a ~50°C gradient over only a ~5 cm span. Few fuel performance codes can perform a cladding burst analysis with adequate fidelity to capture these inherently local effects.

The main objective of this work was to develop and demonstrate an *in-situ* method capable of simultaneously quantifying cladding deformation and thermal gradients during simulated LOCA. Burst testing was conducted with the out-of-cell Severe Accident Test Stations (SATS) located at Oak Ridge National Laboratory, where the experimental process evolved into a modified set up; burst was conducted in air on ~76 mm length claddings. Digital image correlation (DIC) is utilized to quantify dimensional hoop strain during burst, and infrared (IR) thermography to investigate thermal gradients not captured with traditional thermocouple placement. Ultimately, the technique demonstrates that cladding creep strain rate, failure strain, and true stress can be calculated, correlated with temperature, and compared to historical data.

2. Summary of Experimental Design

To observe cladding burst through optical and IR means simultaneously, several modifications to the out-of-cell LOCA test rig were necessary, shown in Figure 2-1, and will be covered in greater detail throughout the report. An IR furnace with a 38 mm viewing chamber bored through the center was used, where the angle between lamps was adjusted to allow unobstructed viewing and IR light focusing from the tungsten lamps. Approximately 152 mm from the viewing port, an IR mirror (Edmund Optics, Part # 64470) on a 45° axis relative to viewing chamber was used to transmit visible light into an optical camera (GT6600) with an attached telecentric lens (TC16M120), and to reflect IR light into an IR camera (FLIR E95). Initial experimentation found the optical camera would saturate from the visible light leaving the viewing chamber, so two polarized visible light filters were placed in between the IR mirror and the camera lens, where the angle between the polarized filters determined total visible light attenuation. However, due to furnace temperature ramping, the intensity of the visible light leaving the furnace was not constant, in effect rendering illumination variable, resulting in DIC pattern drop-off and an over-all lowering of calculatable strain data. Ultimately, an additional modification (not shown in the figure) was introduced, a SiC “C” shaped cell, resolving several IR and visible light illumination issues, and will be described in detail later.

It was necessary to remove the quartz reaction tube rom the testing environment, as the quartz began to emit IR as it heated up, masking the IR signal from the cladding. Without the reaction tube, the experiment could only be performed in air. Differences in Zr oxidation rate in air and steam are marginal, but the mechanical implications of the air environment have not been investigated yet. LOCA testing has traditionally been performed on ~30 cm length cladding tubes [10]. It was not possible to reliably predict where the balloon and burst would occur on a ~30 cm length cladding tubes, and therefore, 76 mm lengths of Zr4 cladding were used, where thick walled 316SS cladding and additional compression fittings were used to center the shortened cladding length in view.

In the following sections, text and discussion is devoted to detailing the technical and physical issues that initially prevented quality in-situ deformation observation, and describes the progress made in the experimental technique. In the final sections, a proof-of-concept demonstration of captured strain and temperature data is given.

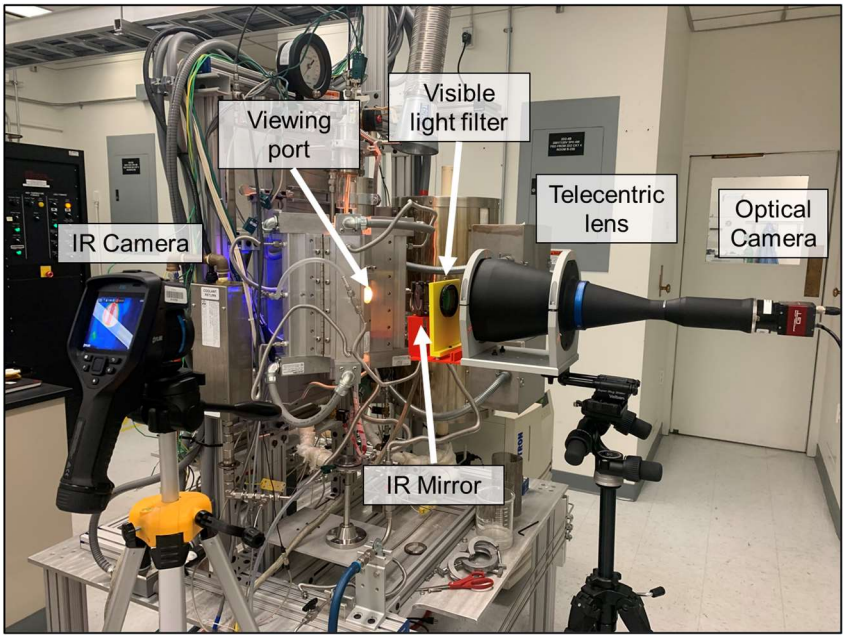

Figure 2-1 Experimental set up with primary components labelled. Over the course of experimentation, some primary components are removed from the set up and will be denoted accordingly.

3. Infrared Thermography

3.1 Planck's Law

The electromagnetic spectrum is broken up into several bands defined by wavelength; gamma, x-ray, ultraviolet, visible, infrared, microwave, and radio waves. Within each band, narrower bandwidth classifications exist. The present simultaneous DIC and IR characterization utilize the visible and IR bands, respectively, shown in Figure 3-1. Thus, a mirror capable of transmitting visible but reflecting IR was used. However, the mirror only reflected IR at a 95% level up to 1.125 μm – mirrors capable of transmitting the visible band and reflecting the *entire* IR band are not commercially available. This issue will be addressed further on.

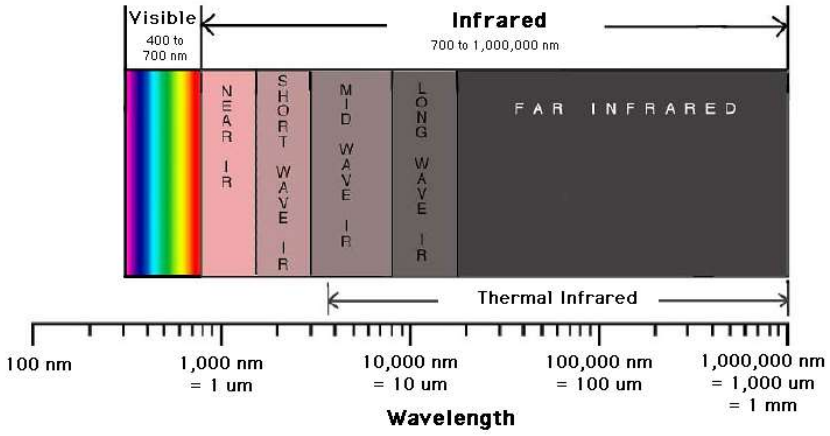

Figure 3-1 Visible and infrared electromagnetic spectrum

A blackbody is defined as (1) an object that absorbs all incident radiation at any wavelength and (2) as an object capable of emitting radiation at any wavelength. The spectral distribution of a blackbody's radiation (emission) is given by Planck's Law,

$$W_{\lambda b} = \frac{2\pi hc^2}{\lambda^5\left(e^{hc/\lambda kT^{-1}}\right)} \times 10^{-6}\left[\frac{Watt}{m^2}, \mu m\right] \qquad (3)$$

where $W_{\lambda b}$ is the blackbody spectral radiant emittance at any wavelength λ (μm), c is the speed of light (3E8 m/s), h is Planck's constant (6.626E-34 J/s), k is Boltzmann's constant (1.4E-23 J/K), and T is the absolute temperature (K). Blackbody spectral radiant emission is plotted as spectral energy density (W/m^3) as a function of both temperature (°C) and wavelength (μm) in Figure 3-2. Spectral energy density is a continuous rather than discrete function, meaning that a blackbody at 1500°C emits at a maximum energy density in the short wave IR band (1-3 μm) but also emits visible light. As blackbody temperature decreases, for instance to 600°C, the wavelength of maximum energy emission increases to mid wave IR (3-5μm). By differentiating Planck's Law, the wavelength λ (μm) of maximum emission for a blackbody at temperature T (K) is approximated by Wien's displacement law,

$$\lambda_{\max} = \frac{2898}{T}[\mu m]. \qquad (4)$$

As the temperature of an object increases or decreases, the wavelength of maximum spectral emission accordingly decreases or increases. By integrating Planck's Law from $\lambda = 0$ to ∞, the total radiant emittance (W_b) of a blackbody is given by Stefan-Boltzmann's law,

$$W_b = \sigma T^4\ [\mathrm{Watt/m^2}], \qquad (5)$$

which states that the total emissive power of a blackbody is proportional to the fourth power of its absolute temperature, multiplied by the Stefan-Boltzmann constant.

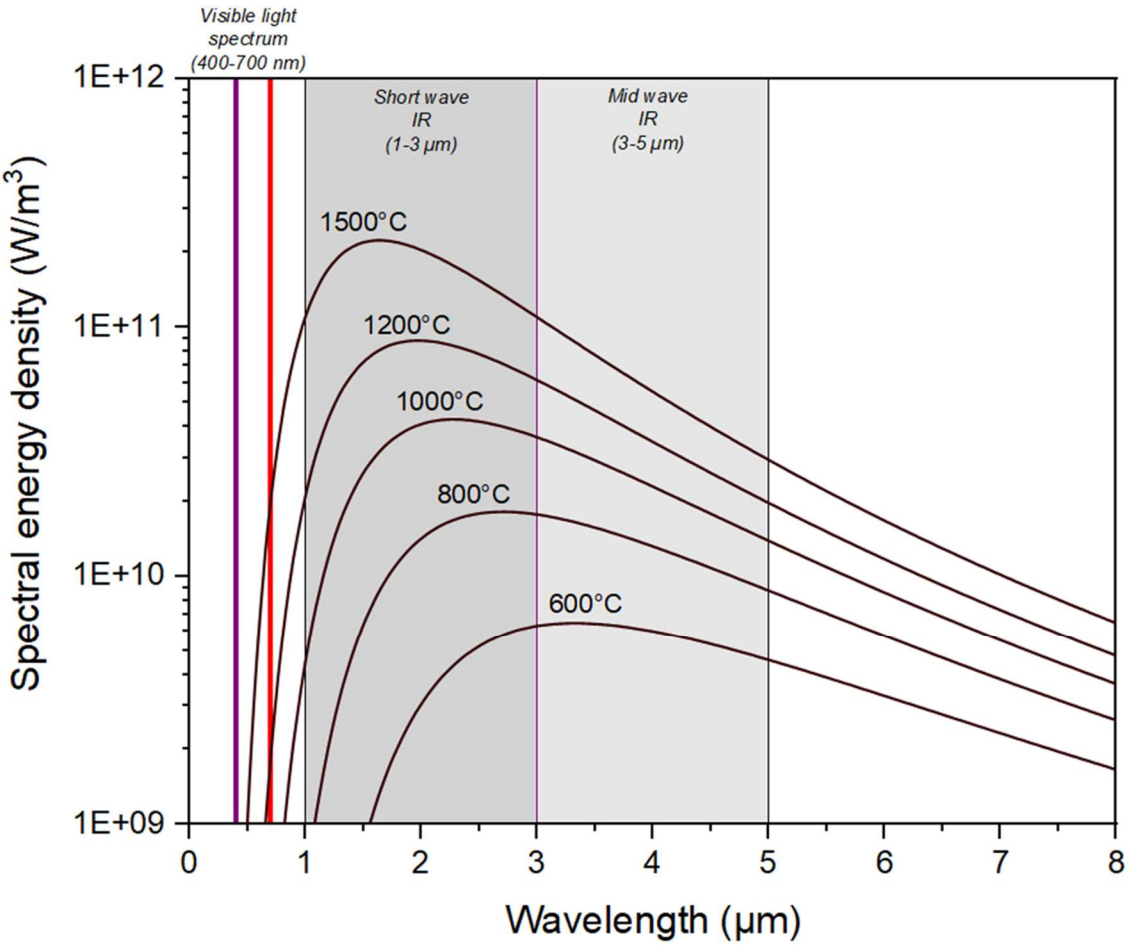

Figure 3-2 Spectral energy density (Planck's Law) of a blackbody's emission as a function of wavelength and temperature.

3.2 Emissivity and IR Reflectivity

The above discussion is informative but limited, as in actuality there are no perfect blackbodies. There are three processes that cause an object to not behave as a blackbody but rather as a graybody: absorption, reflection, and transmission. Consider an object (graybody) with incident spectral power, for instance an object being heated by a tungsten filament IR lamp. The object's spectral absorptance at any given wavelength, α_λ, is the ratio of the incident spectral power from the IR lamp absorbed by the object. The object's spectral reflectance at any given wavelength, ρ_λ, is the ratio of the spectral power from the lamp that is reflected by the object. The spectral transmittance, τ_λ, is the ratio of the incident spectral light that is transmitted through the object. At any wavelength, the ratios sum to unity,

$$\alpha_\lambda + \rho_\lambda + \tau_\lambda = 1. \qquad (6)$$

For opaque materials, where no spectral power is transmitted, $\tau_\lambda = 0$, so that

$$\alpha_\lambda + \rho_\lambda = 1. \qquad (7)$$

This relationship is illustrated in Figure 3-3 for a blackbody and graybody adjacent to a W-filament IR lamp while being observed with an IR camera. For a perfect blackbody, all incident IR radiation is absorbed, and in turn, the blackbody itself emits a spectral distribution, containing IR, proportional to the blackbody's temperature. Thus, the IR signal at the camera is solely the blackbody IR emittance. For a graybody, a portion of the incident IR is reflected off, and the IR signal at the camera is a combination of IR emittance due to the graybody's absolute temperature *and* the reflected IR from the W-filament lamp. According to Kirchhoff's law, for any material, the spectral emissivity, ε_λ, at any specified temperature and wavelength is equal to the spectral absorptance,

$$\varepsilon_\lambda + \rho_\lambda = 1. \qquad (8)$$

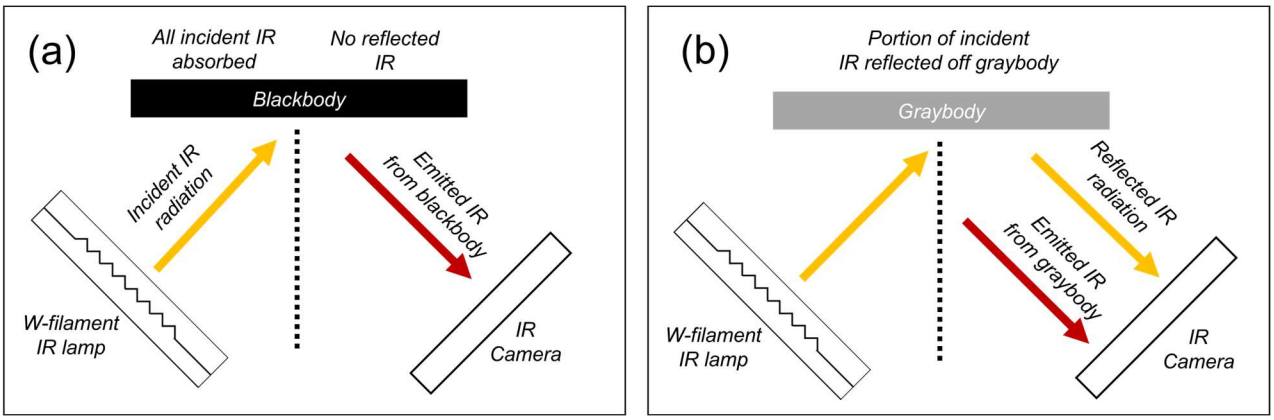

Figure 3-3 Response of a (a) blackbody and (b) graybody object to incident IR radiation from a W-filament IR lamp

The spectral emissivity, ε_λ, is the ratio of the spectral radiant power from an object to that of a perfect blackbody, and is expressed mathematically as

$$\varepsilon_\lambda = \frac{W_{\lambda,object}}{W_{\lambda,blackbody}}, \qquad (9)$$

and qualitatively is a measure of an object's propensity to be a graybody. For a graybody then, the Stefan-Boltzmann equation becomes

$$W_b = \varepsilon\sigma T^4 \ [\mathrm{Watt/m^2}]. \qquad (10)$$

Thus, when quantifying temperature through IR thermography, knowing an object's emissivity across the range of IR relevant wavelengths is critical for accurate measurement. In general, emissivity (and subsequently reflection) is a function of wavelength and can change with temperature. The relationship

between an objects emissivity at a particular wavelength cannot be determined *a priori*, and must be determined empirically. Ceramics tend to have a higher emissivity, while for metals, emissivity commonly hovers around ~ 0.2, where surface finish and the presence of an oxide scale can significantly alter this value; lower for the former, and higher for the latter. However, once an oxide scale of sufficient thickness forms, the emissivity remains constant.

3.3 IR Reflectivity During Burst Testing

Zr4 cladding IR reflectivity has severe implications during burst testing, as cladding heating is provided by four tungsten IR lamps. Details regarding the design of the burst rig are available elsewhere [11] but the presently germane information is graphically illustrated in Figure 3-4. For traditional out-of-cell LOCA burst testing, four IR lamps positioned 90° apart heat the cladding train assembly. The furnace chassis is constructed from polished aluminum and water cooled internally. Each tungsten lamp is situated in an elliptical shell, also made of polished aluminum, that acts as a focusing lens. The estimated incident IR focused beam width of each lamp on the cladding is 3.74 mm. The circumference of a 9.5 mm OD Zr4 tube is 29.91 mm. To observe cladding deformation in-situ, a second furnace was constructed where the angle between lamps was smaller, 72°, allowing a ~38 mm viewing chamber to be bored into the side without significantly altering IR heating optics. The estimated incident IR beam width on the cladding is 4.09 mm. Due to the curved cladding surface and IR reflectivity, the IR signal observed at the viewing chamber is a combination of reflected IR from the two front lamps and the IR emittance from the Zr4 cladding itself. Explicitly, the IR energy used to heat the cladding inhibits accurate IR temperature measurements.

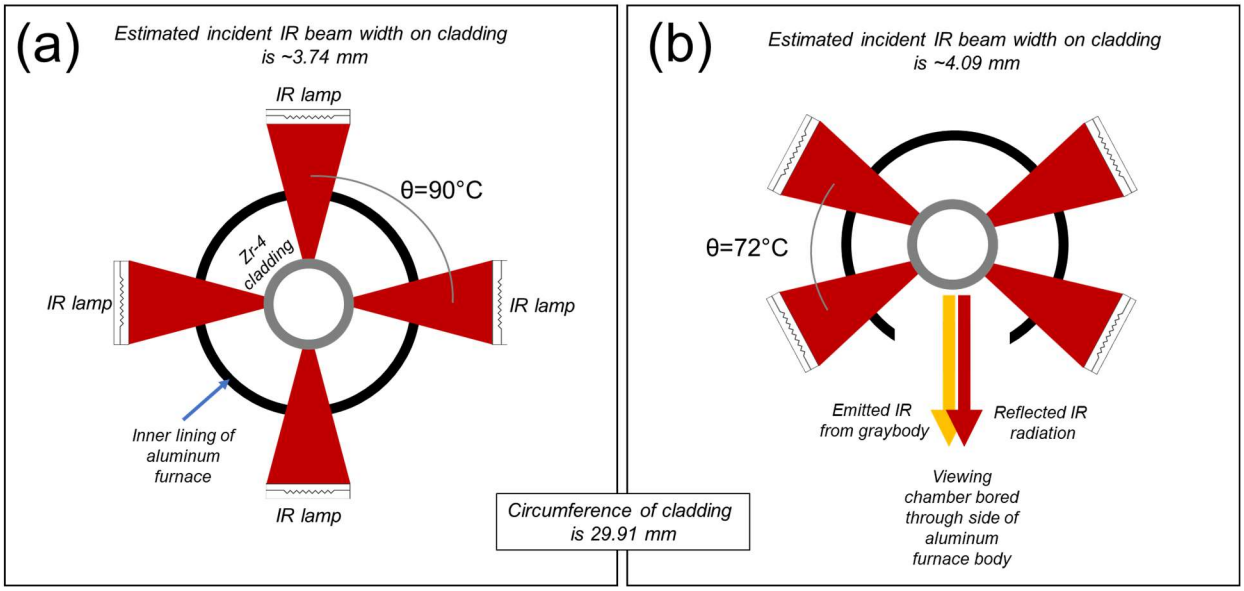

Figure 3-4 Schematic showing the differences in the IR furnaces used (a) previously for standard LOCA burst testing and (b) presently for observing in-situ cladding deformation during LOCA like conditions.

This predicament is shown in Figure 3-5. In the top row, an IR thermal image and associated optical image of pressurized, laser-engraved Zr4 cladding during 5°C/s heating is shown prior to any visible deformation. On the thermal map, 3-5(a), there appears to be a ~ 100°C horizontal gradient across the cladding due to two "hot" bands running down the cladding length. These bands are the direct IR reflection from the IR lamps, and also a visualization of where direct heating occurs. Spectral contributions from reflected and

emitted IR can be parsed and calculations made to account for the reflected contribution, but this requires the temperature source of the reflected IR to be known precisely. At full output, the tunsgten lamps can easily surpass 2000°C, well beyond the temperature capabilities of the IR camera (~1500°C). Furthermore, the parsing calculations basic assumption is that the reflected IR source is at a relatively low temperature or power, for instance, accounting for reflected sunlight or halogen-bulb light off a car engine. The "cooler" band running down the cladding length in 3-5(a) is actually reflecting off ambient IR incident from the viewing chamber (i.e. the room outisde the furnace). Here, in theory, cladding temperature can be accurately measured with IR means. However, once significant ballooning begins, Figure 3-5(c) and Figure 3-5(d), there isn't sufficient resolution to clearly distinquish the band due to the lamp's IR reflection becoming thicker. It's presently unclear if these observed horizontal gradients are real or even possible. Nonetheless, any method attempting to correlate strain with temperature should minimize the gradient, if real, or eliminate the IR reflections.

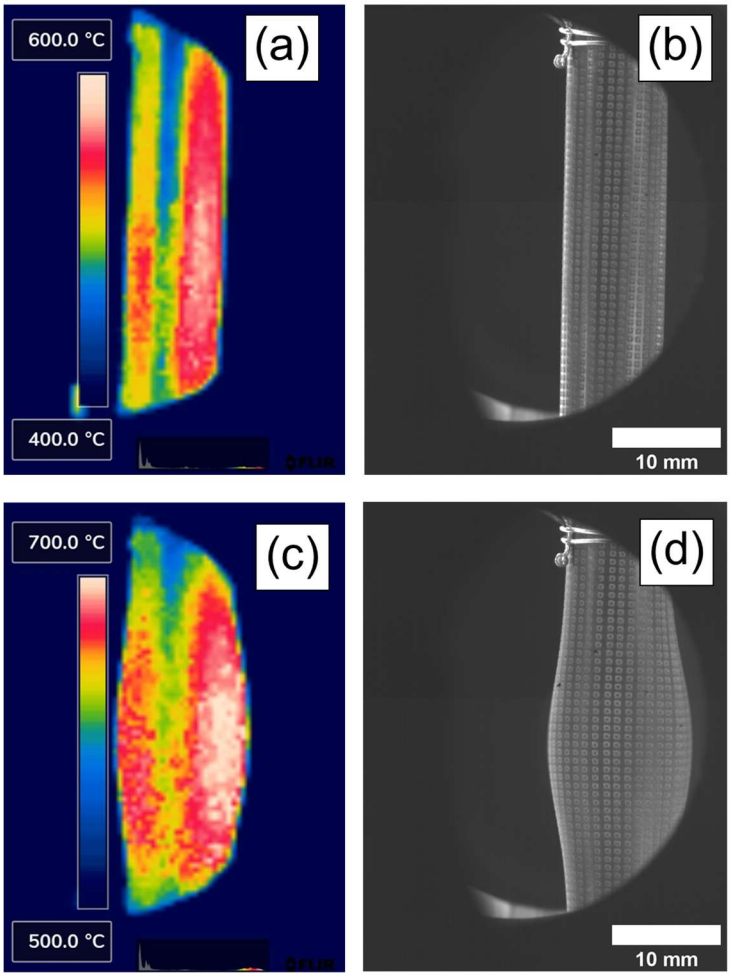

Figure 3-5 (a) IR thermal map and (b) optical image of pressurized Zr4 cladding during 5°C/s heating prior to visible deformation and (c) IR thermal map and (d) optical image of cladding immediately prior to burst.

3.4 Implementation of SiC "C' Shell to eliminate IR reflectivity

To block the direct IR irradiation of cladding during burst, a SiC "C" shell (Hexoloy SA) was introduced into the cladding train assembly. The shell conceptually illustrated in Figure 3-6(a). Implementation into the cladding train assembly is shown in Figure 3-6(b). To center the 76 mm length Zr4 cladding in front of the viewing chamber, 76 mm thick walled 316SS extension claddings were used on the top and bottom of the assembly, with the top extension being terminated with a compression fitting and high-pressure line, and the bottom extension being terminated with a compression fitting but fixed at the bottom of the furnace. Both extensions contain a 316SS rod running through them to mimic the internal occupied volume of a 30 cm length cladding. During traditional LOCA testing, 316SS centering rings are welded onto the OD of the compression fittings to center the cladding assembly in a quartz reaction tube. Here, the centering rings serve a similar purpose, preventing contact with the aluminum chassis of the furnace, but also provide a platform for the SiC shell to rest during testing. Two thermocouples were used during testing, $T_{Control}$ and T_{Sample}. The heating profile is controlled via LabView and is based off $T_{Control}$. Through experimentation, it was determined that $T_{Control}$ cannot be shielded from direct lamp IR; the furnace element controllers would often over or undershoot temperatures. Therefore, $T_{Control}$ was fixed to a compression fitting facet outside the shell, and secured with Type-B thermocouple wire to the top centering ring. T_{Sample} was secured in a similarly, and bended in such a manner as to have the TC bead in direct contact with the cladding and visible through the viewing chamber. Thus, T_{Sample} is a temperature reading of the top portion of the cladding, with the absence of any direct IR heating, and no cladding constriction due to thermocouple securement. An optical macrograph through the viewing chamber of the modified cladding train assembly is shown in Figure 3-6(c).

In previous studies utilizing 30 cm length Zr2 claddings, four thermocouples were used to span the center ~ 10 cm of length, with three thermocouples on the back side of the cladding, and one in the front. Large thermal gradients were measured, typically 50-100°C horizontally and vertically, yet replicate testing found excellent agreement in burst pressures and temperatures. The large gradients may be an artifact of differential IR heating rates between alumina thermocouple sheaths, thermocouple weld/bead, and cladding, as each material differs in emissivity/reflection. The discontinuous circumferential heating (Figure 3-4) present in the furnace may also contribute; if a TC bead rests in a focused IR beam width, it may read differently than when not.

With the SiC shell, there's no direct IR heating of the Zr4 cladding. Instead, both the top and bottom 316SS extensions, which are not shielded from the IR lamps, conductively heat the cladding. Additionally, and perhaps to a larger effect, the SiC shell acts as a heat source; SiC is a common furnace heating element. With a relatively high emissivity (~0.8-0.9) and being fully exposed to four IR lamps, the SiC shell will heat rapidly and be a heating element in close proximity with the Zr cladding.

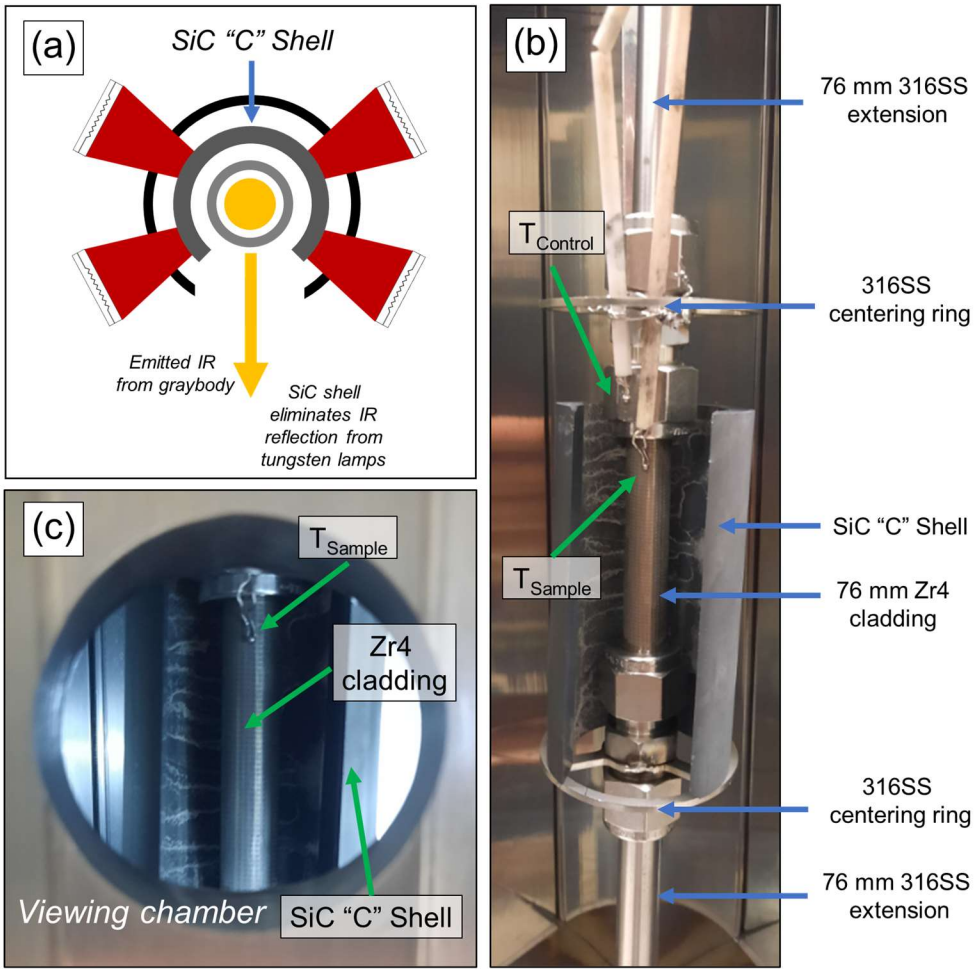

Figure 3-6 (a) Conceptual illustration of a SiC "C" shell blocking direct IR radiation of cladding during burst testing. (b) Macrograph of cladding train assembly utilizing 76 mm Zr4 cladding length and SiC "C" shell. (c) Optical image showing assembly sitting in furnace through the viewing chamber.

To investigate the thermal implications of the shell, an unpressurized Zr4 cladding in an assembly shown in Figure 3-6(b) was taken through a series of isothermal holds, set by $T_{Control}$, spaced 100°C apart. IR images were taken in two camera configurations, the first being directly in front of the viewing chamber, and the second utilizing the IR mirror. Upon $T_{Control}$ reaching the isothermal temperature, 10 min passed to allow thermal equilibrium, and T_{Sample} was recorded, along with the IR images of the two camera configurations. Over 300° to 1000°C, T_{Sample} was consistently ~40°C lower than $T_{Control.}$ An optical macrograph showing IR camera point of view when positioned directly in front of the viewing chamber is shown in Figure 3-7(a), and the associated IR camera image in Figure 3-7(b), with $\varepsilon = 0.9$. Due to the shell reaching higher temperatures than the cladding, the border between shell and cladding is obscured. In general, the shell and cladding contrast decreased with increased temperature. However, no bright bands were visible on the cladding, meaning the shell successfully blocked direct line-of-sight to the IR lamps. Furthermore, temperature was fairly uniform from top to bottom, the bottom being ~40°C cooler and the gradient roughly linear.

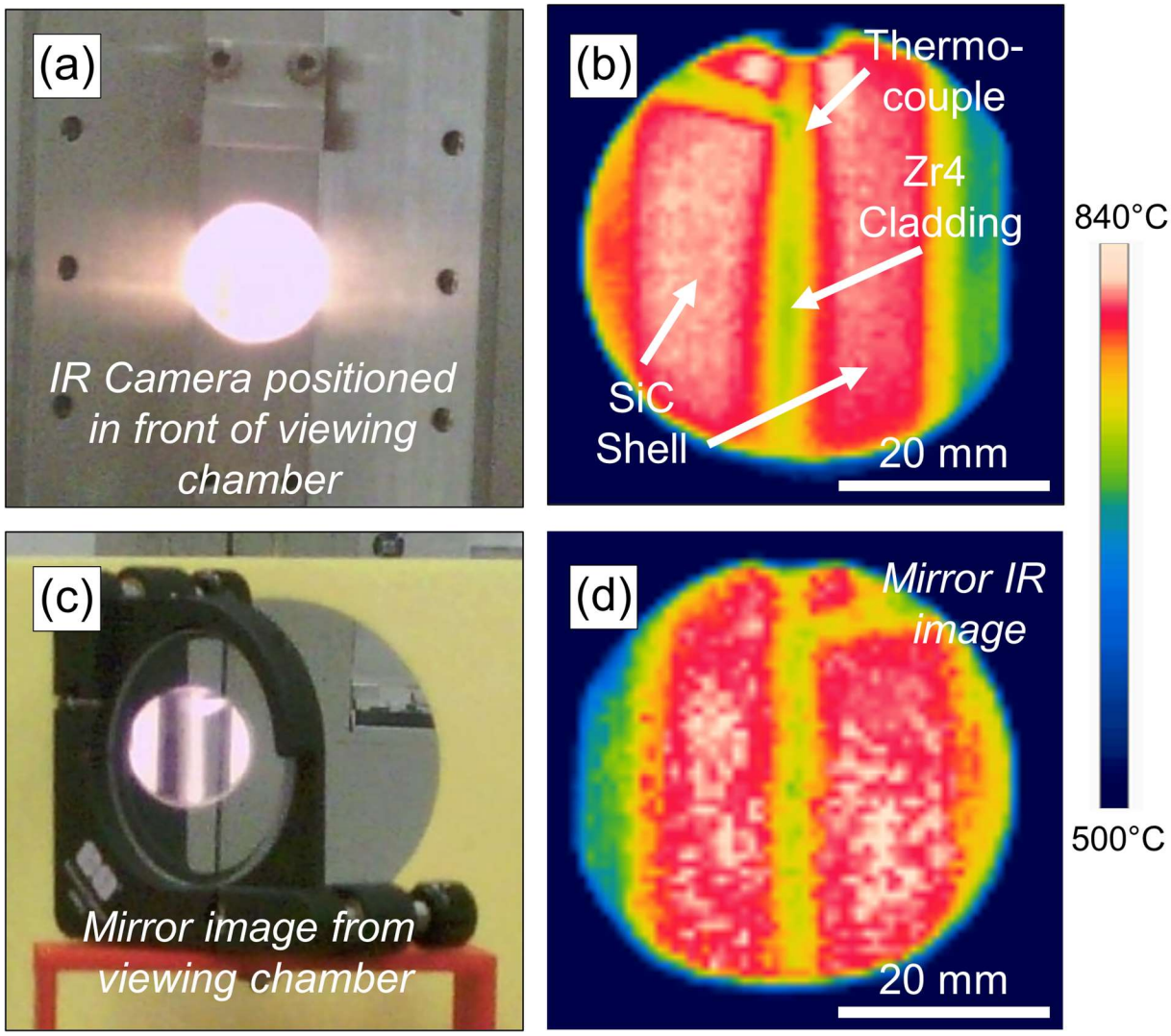

Figure 3-7 (a) Macrograph showing IR camera point-of-view when positioned directly in front of the viewing chamber and (b) associated IR image of un-pressurized Zr4 cladding when T_{Sample} = 757°C. (c) Macrograph showing IR camera point-of-view when observing viewing chamber with IR mirror and (d) associated IR image, also when T_{Sample} = 757°C.

IR image clarity was significantly reduced utilizing the IR mirror, Figure Figure 3-7(c) and Figure 3-7(d). Furthermore, it was necessary to adjust the IR camera settings to match the temperature readings of the direct line-of-sight configuration. Specifically, it was necessary to implement a 10% transmission coefficient, meaning the IR calculation would intake the incoming IR signal as being only 10% of the total being emitted, and adjust accordingly. Over the 500° to 800°C temperature range, the transmission coefficient necessary to match the mirror and straight-on thermal readings was consistently 0.1, meaning the IR mirror only reflected ~10% of the emitted IR that temperature range. This relationship is shown in Figure 3-8(a), where the specified transmission and reflection coefficients of the IR mirror are represented

by shaded grey boxes. Over the visible light band, 85% of light is transmitted through the mirror into the optical camera, while in the 0.79-1.13μm near IR band, 95% of the IR is reflected off. On the right axis, and shown by a red curve, the relationship between a blackbody's wavelength of maximum emission and temperature (Wien's displacement law) is shown, where present LOCA relevant temperatures are indicated by the shaded green box. The experimentally determined reflection coefficients of the IR mirror in the 2-5 μm band are represented by blue squares. Ideally, for LOCA relevant temperatures, the IR mirror should be capable of reflecting in the 2-5 μm range. However, mirrors capable of transmitting visible and reflecting IR up to 5 μm are not commercially available. In the LOCA relevant range, the presently used IR mirror only reflects ~10% of the cladding's emitted IR signal. In theory, it may be possible to place an IR mirror reflective in the entire 1-10 μm range in the same plane as the lens, and placing the IR camera adjacent to the furnace, thereby eliminating the need to split the viewing chamber image into optical and IR components. Additionally, if a smaller telecentric lens could be used, the IR camera could be placed adjacent to the lens, so that both optical and IR cameras are viewing directly into the chamber.

With the elimination of IR reflection off the cladding surface, it was possible to experimentally determine the emissivity of Zr4 as a function of temperature. This was done with the IR camera directly in front of the viewing chamber, similar to the process described with Figure 3-7. The furnace was taken through a series of isothermal holds at centennial intervals, and 10 min passed to allow thermal equilibrium. Then, emissivity on the IR camera was adjusted so that the IR reading in the vicinity of T_{Sample} was in relatively good agreement with the thermocouple measurement. The difference between the thermocouple and IR camera reading is shown on the left axis of Figure 3-8(b), and emissivity is plotted on the right axis. At 100°C, an emissivity of ~0.94 was necessary to match the temperature readings, decreasing to 0.88 at 850°C. These emissivity values agree with [12] but are not agreement with generally accepted emissivity values of metals prior to oxidation. According to literature reports, emissivity of smooth, unoxidized Zr4 cladding should be closer to ~0.2-0.3 [13], [14]. However, oxides as thin as 2 μm can significantly change emissivity [15], and it's accepted that as zirconium based alloys oxidize, emissivity rises to ~0.9 [16]. It may be that the cladding is either sufficiently oxidized in the as-received condition, or that at 100°C a macroscopically invisible oxide of sufficient thickness forms and raises cladding emissivity from the ~0.2-0.3 range to ~0.9.

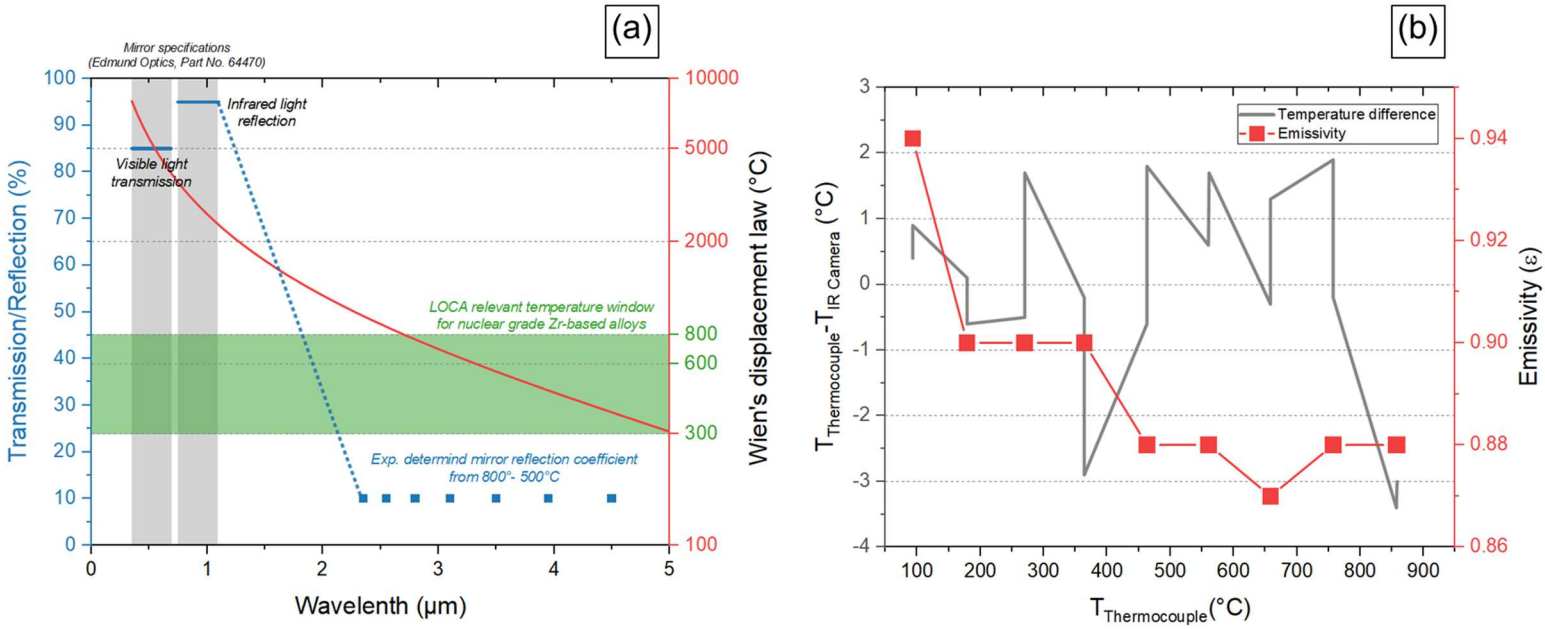

Figure 3-8 (a) Visible light transmission coefficient and IR light reflection coefficient of the IR mirror. The mirror specifications are highlighted by grey shaded boxes, while the experimentally determined reflection coefficient over the 500° to 800°C range is shown by blue squares. On the RHS axis, the relationship between maximum wavelength emittance and temperature of a black body is shown (Wien's displacement law). (b) Necessary emissivity to match direct line-of-sight IR camera temperature to cladding temperature (T_{Sample}) determined with a thermocouple.

4. Digital Image Correlation

In-situ 2-dimensional DIC was performed with an optical camera and telecentric lens. The telecentric lens, with a focus depth of 15.8 mm, ensured the entirety of the cladding was focused. To briefly summarize DIC, a reference image of a pattern is taken, where the spatial evolution of the individual objects comprising the pattern is used to calculate strain. For LOCA burst testing, it was critical to utilize a patterning method capable of withstanding high temperatures. The first several iterations attempted to use high temperature Cr_2O_3-based paint to draw a stochastic variable thickness dot pattern, but were ultimately unsuccessful, as the chromia based pattern had a propensity to "bleed" out across the cladding surface during temperature ramping. An alternative method which utilized glass-based white and black paint was considered, but was not attempted due to concerns about what impact a glassy layer would have on observed strain.

Instead, a laser engraved pattern was chosen, which had previously demonstrated promising results during earlier investigations [Garrison et al.]. A single-pass square pattern, shown in Figure 4-1(a), was inscribed onto Zr4 cladding with a laser engraver operating at 20 kHz and 20 Watts (TYKMA electrox BOQX laser engraver). The middle 60 mm of each 75 mm tube specimen was engraved with 36 rows (10 degrees of circumferential rotation between each row) of a repeated square pattern in the axial direction. Each square

was 400 x 400 µm, and the spacing between each square was 400 µm edge to edge. The engraving depth was measured on a Keyence-5000 structured light scanner, where the maximum depth was found to be ~25 µm. Cross sectional microscopy will be conducted in the future to not only better quantify Zr4 engraved depth, but to investigate crack propagation behavior. The inscribed pattern may hinder the intrinsic Zr4 mechanical integrity but the approximated depth is only ~ 4.3% of the Zr4 cladding wall thickness (nominally 575 µm).

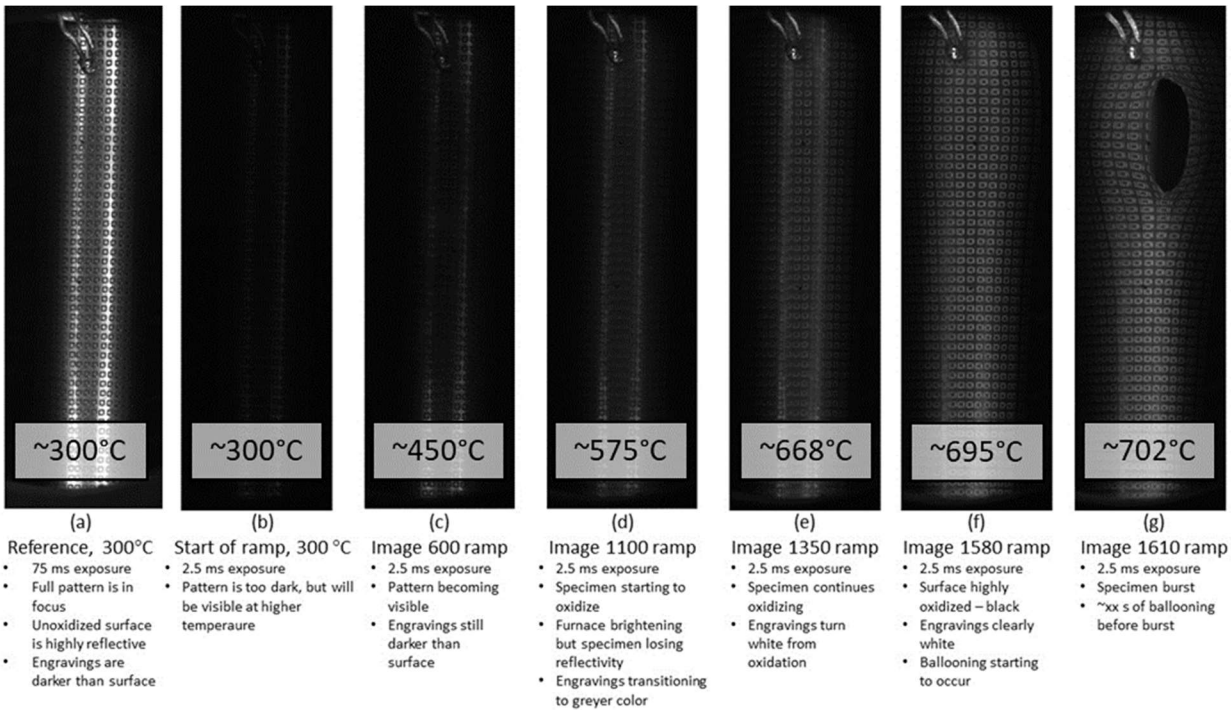

Figure 4-1 (a) Reference DIC image and (b)-(c) a series of optical images taken during 300° to 1200° temperature ramping. Estimated temperatures, determined from the thermocouple in the top regions of each image, are overlaid.

A series of optical images taken during a 1°C/s ramp from 300° to ~702°C at rate of 4 frames-per-second (FPS) is also shown in Figure 4-1(b)- in Figure 4-1(g). The initial reference image, Figure 4-1(a), was taken during a 300°C 10 min isothermal hold that precedes the temperature ramp. Prior to SiC shell implementation, the use of two visible light filters in conjunction with varying camera exposure were necessary to obtain sufficient cladding illumination throughout ramping. However, with the SiC shell, the visible light filters were removed from the experiment, and only exposure changes were necessary. The reference image was taken with a 75000 µs exposure, then the exposure was changed to 2500 µs. The immediate lowering of pattern clarity when exposure is decreased is clear in comparing Figure 4-1(a) and Figure 4-1(b). As temperature increases (i.e. the tungsten-filament lamps burn brighter) total illumination increases, and the series of optical images becomes increasingly clear. Prior to burst testing, unpressurized, fresh claddings were taken through a series of temperature ramps to determine the optical exposure parameters for proper illumination in the 500° to 800°C temperature range, where cladding deformation began. Seen in the series of optical images, the reflectivity of the cladding surface appears to decrease over the exposure. This may be due to changes in the overall optical specifics or oxidation decreasing cladding luster. However, the empirically determined emissivity necessary to match IR thermal readings with thermocouple readings, Figure 3-8(b), decreased as temperature increased, implying that reflectivity should increase with temperature. This phenomenon will be investigated further in future studies.

Regarding frame rates, the DIC calculation becomes increasingly arduous with increased image frequency. Fortunately, frame rate can be adjusted during data collection. As a nominal example, the camera could operate at 0.5-1 FPS during the lower temperature segment of the ramp, and increase to 2-5 FPS when cladding deformation begins, and potentially beyond 10 FPS in the moments immediately prior to burst to observe burst opening initiation and evolution.

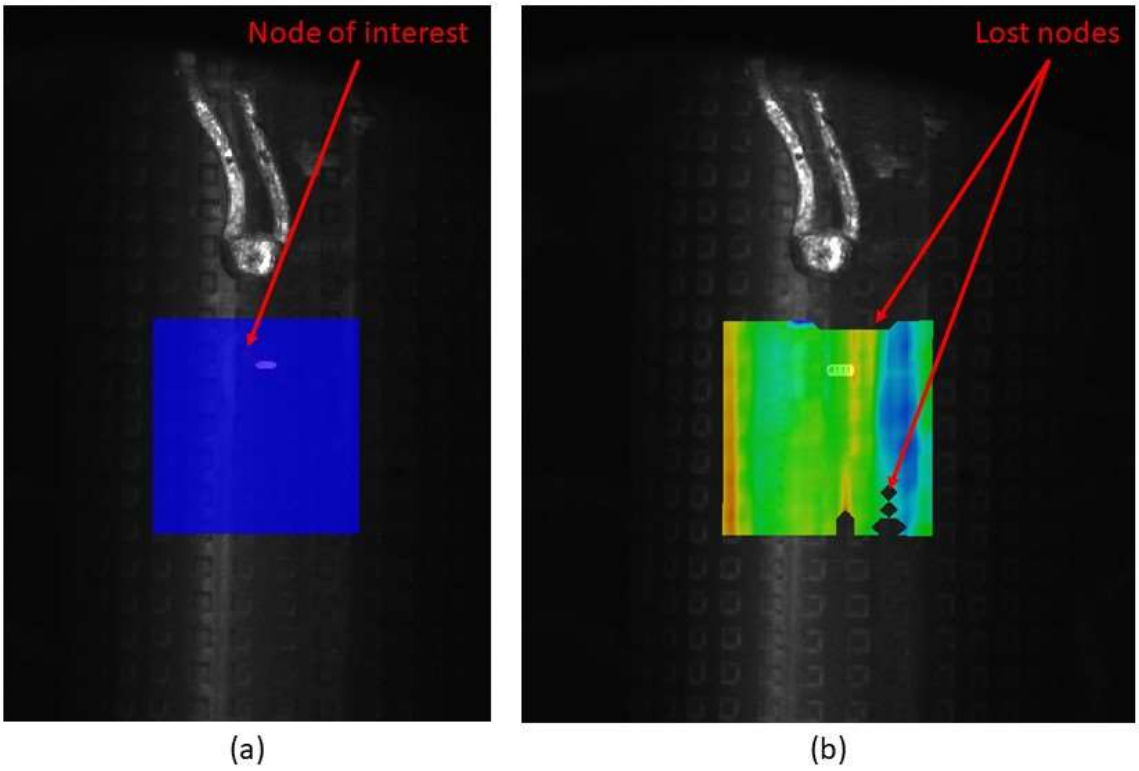

Figure 4-2 The DIC field placement (a) the reference image (image # 715) showing the node of interest and (b) image 885 showing loss of tracking for several nodes.

DIC images were analyzed with Ncorr open-source DIC algorithms [17] to calculate hoop and axial strains. To account for the changes in light intensity and specimen/pattern oxidation, a DIC approach that updated the reference image was utilized in this work. Specifically, DIC images were loaded into the software starting with the first image that was visible (Figure 4-1(c) above) as the reference image. A field of 105-pixel objects were created in a grid with 10-pixel spacing near the thermocouple. An example of this field placement is shown in Figure 4-2(a), where the node of interest is highlighted because it is the closest to the thermocouple without its 105-pixel object being obstructed by it. For reference, one engraved square on the pattern had a width of ~30 pixels. Steadfast tracking that allows the system to update subsets and increases the number of allowed iterations was also selected. After the field is created, the DIC object tracking is started, which calculates strain and displacement in later images compared to the reference image. However, due to the changing light/pattern, the software would lose tracking of the object when it could not trace the current image back to the reference image. This is shown in the software by nodes being removed from the field calculation, as shown in Figure 4-2(b). When any node near the node of interest was dropped due to lack of DIC tracking, the procedure was stopped, and the strain data was output for the

node of interest up until the image that tracking was lost. Then a new DIC calculation was started using the image 5 images prior to the lost-tracking image as the reference image, and the process was repeated until specimen burst. Then, to update strain values, the strain values in the new section of strain analysis were shifted such that the strain value of the 5th image in the new analysis (which coincided to the same time as the last image of the previous section) was equal to the average value of the strain of the 5 previous values. For later images when the strain rate was higher, the average of 3 strain values was used. The Hencky (or true strain) values were output, allowing incremental strains from an already-deformed reference image (the updated references would have deformation). It should be noted that updating the reference image would propagate any errors associated with noise or heat mirages. The average of the 5 strain values was used to mitigate these errors, but the use of a more advanced reference-image-updating algorithm like that used by Pan *et al.* [18] would be beneficial to better mitigate or quantify error. No modification to images or strain data was performed to account for specimen curvature, temperature variation, or curvature change due to non-uniform ballooning. The current procedure is expected to be acceptable because the error due to specimen curvature along the centerline of the specimen was determined to be ≤250 με for a speckle-patterned DIC specimens by Cinbiz *et al.* [19] Furthermore, the object size is a square with a width of ~1.4 mm so temperature variation and curvature change are not expected to be significantly large, although the IR temperature map and an updated procedure similar to that in [19] could be performed in the future to specifically quantify the temperature variation and error due to curvature change respectively.

Radial strains, which cannot be calculated through DIC of the tube outer surface, were calculated assuming that volume is conserved, which in general is only realized under plastic deformation [20]. Since plastic deformation is high relative to the elastic portion during the ballooning and burst, the calculation is justifiable, although post-burst measurement of the wall thickness (which can be used to calculate plastic radial strain) or plastic portions of the circumferential and axial strains would be useful to properly quantify the radial strains.

5. In-Situ Observation of Cladding Deformation during Burst

5.1 Experimental details

The previous sections have outlined the transition from the traditional LOCA experiment to the modified experiment that allowed in-situ observation of cladding deformation. Work is on-going to further refine the test methods. In the following sections, the modified experimental set-up was used, and burst testing was performed to demonstrate proof-of-concept. Specifically, laser engraved 76 mm length Zr4 cladding train assemblies were used in conjunction with the SiC "C" shell, shown in Figure 3-6(b), and all experiments were conducted in air. During simulated cyclic dryout experiments [21], maximum heating rates were material specific but generally were within 15-17°C/s. With the SiC shell, cladding temperature (T_{Sample}) lags the control temperature ($T_{Control}$) due to IR shielding of the cladding (see Figure 3-6), where both temperatures are determined via thermocouple. Thorough experimentation is needed to investigate the maximum heating rates but preliminary trials suggest a ~4-5°C/s rate is possible . For the following tests, a 1°C/s heating rate was used, which was found to be highly reproducible.

Although IR image clarity suffered greatly from IR mirror utilization, the general test configuration of Figure 2-1 was used without any visible light filters. An added benefit of the SiC shell was a more consistent illumination level throughout testing, where the optical camera's exposure parameters were sufficient for level adjusting.

5.2 Burst Test at Nominal Initial 8.2 MPa Overpressure

5.2.1 Temperature/Pressure Profile and Burst Hoop Stress

Prior to testing, cladding train assemblies are tested for hermeticity at room temperature with a ~5.5 MPa overpressure, utilizing leak detection fluid at all compression fittings. Nominal initial overpressure, ~8.2 MPa, was set at room temperature, then assembly was isolated from the pressurizing gas cylinders (closed valve). The temperature and pressure profile during burst testing of a 76 mm length Zr4 cladding with a ramp heating rate of 1°C/s at a nominal initial overpressure of ~8.2 MPa is shown in Figure 5-1(a). The cladding train assembly were heated to 100°C rapidly, then to 300°C at 1°C/s and held for 10 min to allow thermal equilibrium, an approximately 5 min longer hold than traditional burst testing. The SiC shell adds considerable thermal mass to the furnace environment, and provides additional means of heating. In order to achieve reliably reproducible heating rates, it was deemed necessary to allow T_{Sample} to reach a steady-state temperature prior to initiating the 300° to 1200°C ramp. After the 10 min hold at 300°C, temperature was then increased to 1200°C at 1°C/s. During this ramp, $T_{Control}$ increased at a 1.01°C/s rate, and T_{Sample} increased at a 0.95°C/s rate.

Internal rod pressure, measured with a transducer residing outside the furnace environment, changed accordingly, increasing rapidly during the 100° to 300°C ramp, slightly during the 300°C hold, and then initially rapidly but at a consistently decreasing rate during the 300° to 1200°C ramp. The pressure increases generally follow an ideal gas law behavior but the system volume and gas pressure is not known. To simulate the internal occupied volume and thermal mass of fuel cladding, a 76 mm length and 8 mm OD alumina rod is contained within the Zr4 cladding. It's anticipated that the internal alumina rod temperature may lag the external cladding temperature during ramp, meaning that the measured external temperatures monitored with thermocouples may not accurately reflect internal gas temperature. Moreover, the total number of gas molecules within the cladding train assembly hasn't been extensively examined, and there are segments of high pressure line leading to the transducer outside the IR furnace. In the present testing, the cladding train assembly length (extensions, cladding, extension internal rods, cladding internal rod) has been normalized, and future efforts will quantify total gas molecules, *n*, which will be advantageous for modelling burst.

A smaller scale pressure and temperature profile centered around the burst event is shown in Figure 5-1(b). Burst time, 1244.1 s, is signaled by the sudden drop in pressure. The coinciding drops in both $T_{Control}$ and T_{Sample} are due to the burst event itself. In theory, an instantaneous increase in ambient gas pressure due to burst could cool the immediate environment, but also, the general behavior of thermocouples is to briefly read a cooler temperature when physically disturbed to a sufficient degree. Regardless, T_{Sample} at 1244.1 is taken as the burst temperature, T_{Sample}= 702°C, which is only slightly cooler than the $T_{Control}$ (which resides outside the SiC shell) temperature of 734°C.

As mentioned above, the rate of cladding internal pressure increase changed during the 300° to 1200°C ramp. At an approximate T_{Sample} temperature of ~650°C, internal pressure reaches a local maximum, then begins to drop at ~675°C, and continues to decrease as the cladding balloons. Because the pressurized cladding is isolated, any significant volume change accordingly decreases internal pressure. The ballooning event was clearly seen through optical means, and the spatial-time progression agreed well with the monitored pressure behavior, seen in the next section.

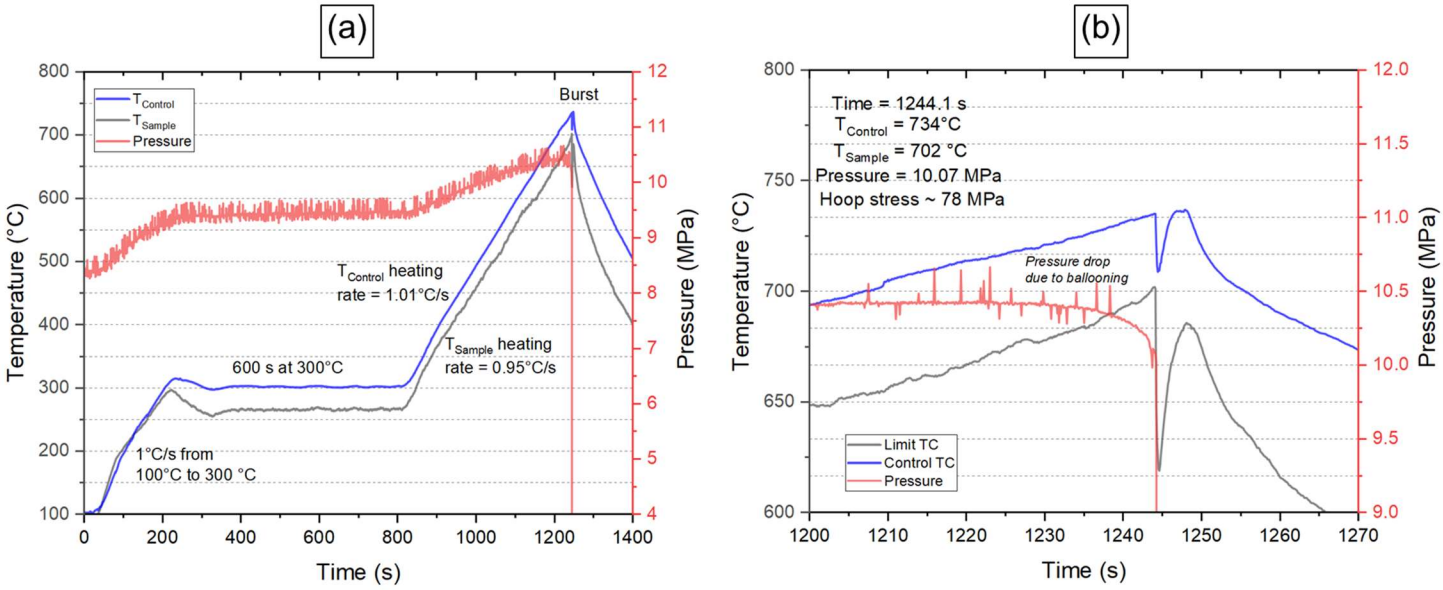

Figure 5-1 (a) Temperature and pressure profile during burst testing of 76 mm length Zr4 cladding in air with a 1°C/s heating rate. (b) Close up of profile when burst occurred.

The burst pressure was 10.07 MPa in Figure 5-1(b), with a calculated hoop stress of ~78 MPa at 702°C. The data is plotted in Figure 5-2, where the relationship between burst hoop stress and burst temperature is shown for Zr4 cladding of varying lengths and heating rates. Historical data from Champan's studies [6], [22] is used as a reference line for comparing burst behavior. The 305 mm length experiments were performed in a traditional LOCA experiment (quartz reaction tube, steam environment, 5°C/s heating rate), while the 76 mm were performed in air, with the SiC shell modification and at 1°C/s.

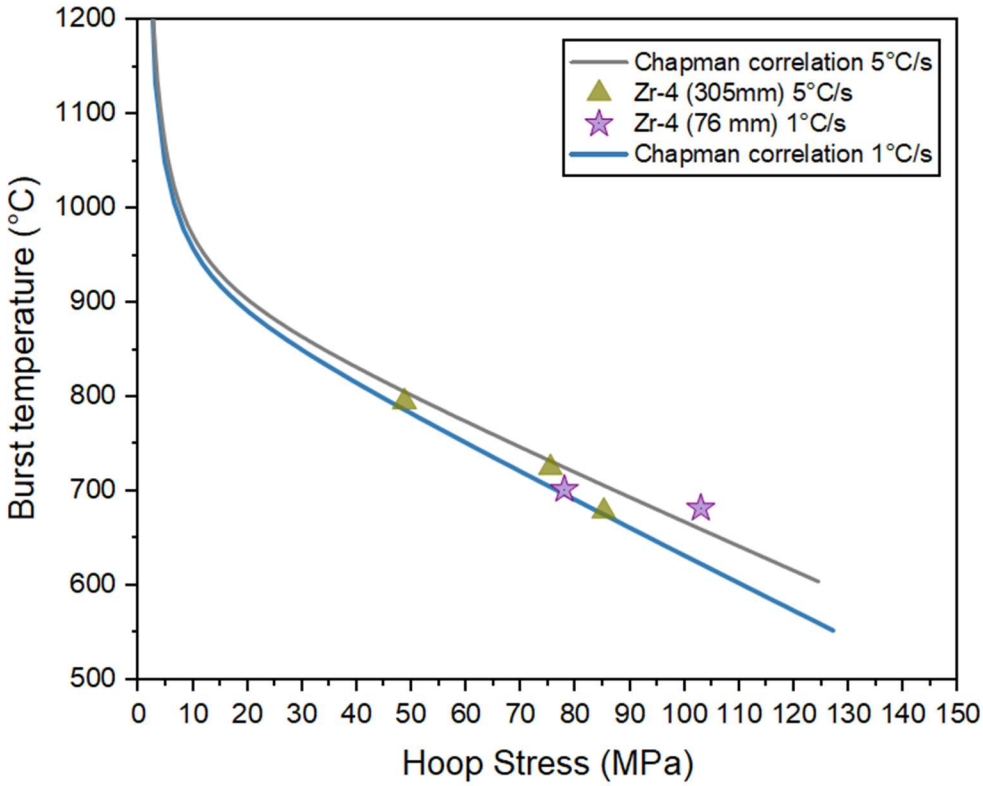

Figure 5-2 Relationship between burst hoop stress and burst temperature of Zr4 cladding with vary lengths and heating rates.

Diametrical measurements were taken along cladding length and normalized to initial diameter (9.5 mm) to indicate strain. Diametrical strain measurements for 76 mm and 305 mm cladding lengths burst at similar temperatures but differing heating rates and gas environments are shown in Figure 5-3(a) and associated optical macrographs in (b) and (c). The ballooning behavior between the 76 mm (1°C/s) and 305 mm (5°C/s) was significantly different, with the former exhibiting much higher diametrical strains. However, the burst region occurred in the vicinity of the compression fitting for the 76 mm length cladding. Clearly, the compression fitting has some role in cladding deformation. Aside from fitting interaction, the increased ballooning at 1°C/s is attributed to there be more allotted time for creep prior to final burst. For the most representative *in-situ* strain measurements with DIC, it will be necessary to ensure burst occurs in the center region of the axial cladding length rather than the fitting vicinity. Also, the mechanical implications, if any, of testing in air as opposed to steam are not understood yet. Burst length (along axial direction) and burst width (along hoop direction) were measured via image analysis and measurements are superimposed onto the respective macrographs. Due to the significant differences in ballooning, burst opening characteristics cannot be directly compared. Furthermore, the implications of the laser engraved pattern on opening initiation and propagation have not been thoroughly investigated.

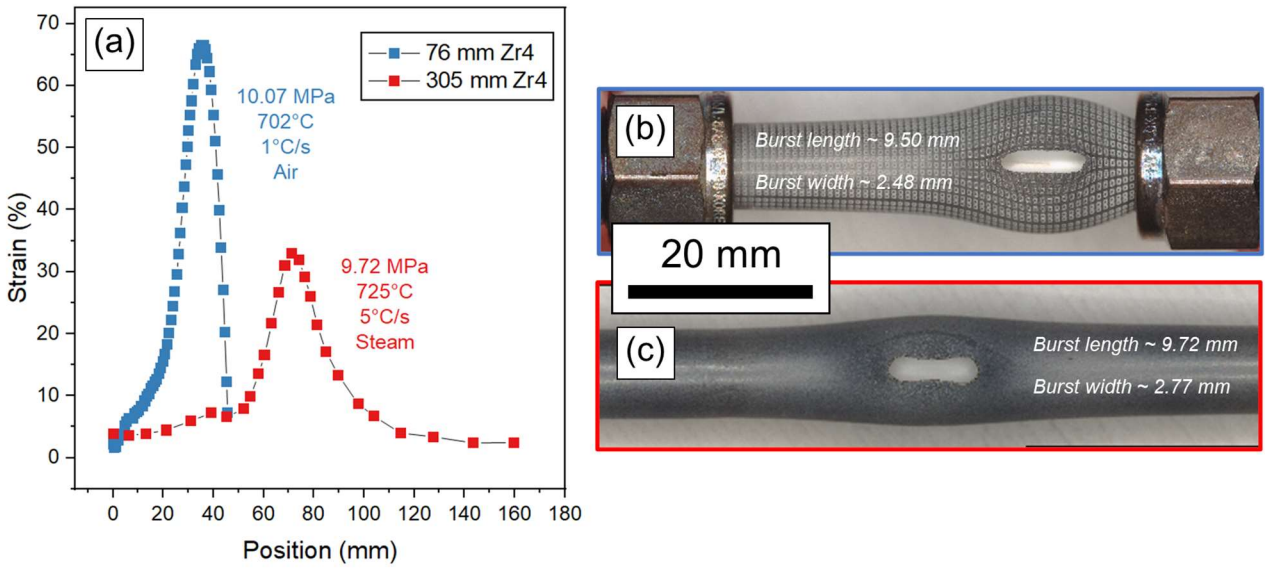

Figure 5-3 (a) Diametrical strain along cladding length of (b) 76 mm and (c) 305 mm length Zr claddings burst at similar temperatures but with differing heating rates and gas environment.

5.2.2 Optical Observation of Cladding Deformation

A series of images taken with the optical camera over the time spanned in Figure 5-1(b) are shown in Figure 5-4. Over the 48 s span, cladding illumination was consistent and spatial resolution sufficient for DIC calculation of strain. The cladding begins to noticeably deform and swell at ~1228 s (~678°C, ~10.4 MPa) in agreement with the internal cladding pressure beginning to drop ~1230 s in Figure 5-1(b). Over the last 8 s prior to burst, significant ballooning occurs, also evident by the decrease in internal pressure. As previously alluded to, implementation of the SiC shell resulted in a more consistent illumination level through the temperature ramp, prior to, and during burst. Over the course of experimentation, burst openings exhibited a tendency to initiate and propagate along the laser-engraved pattern.

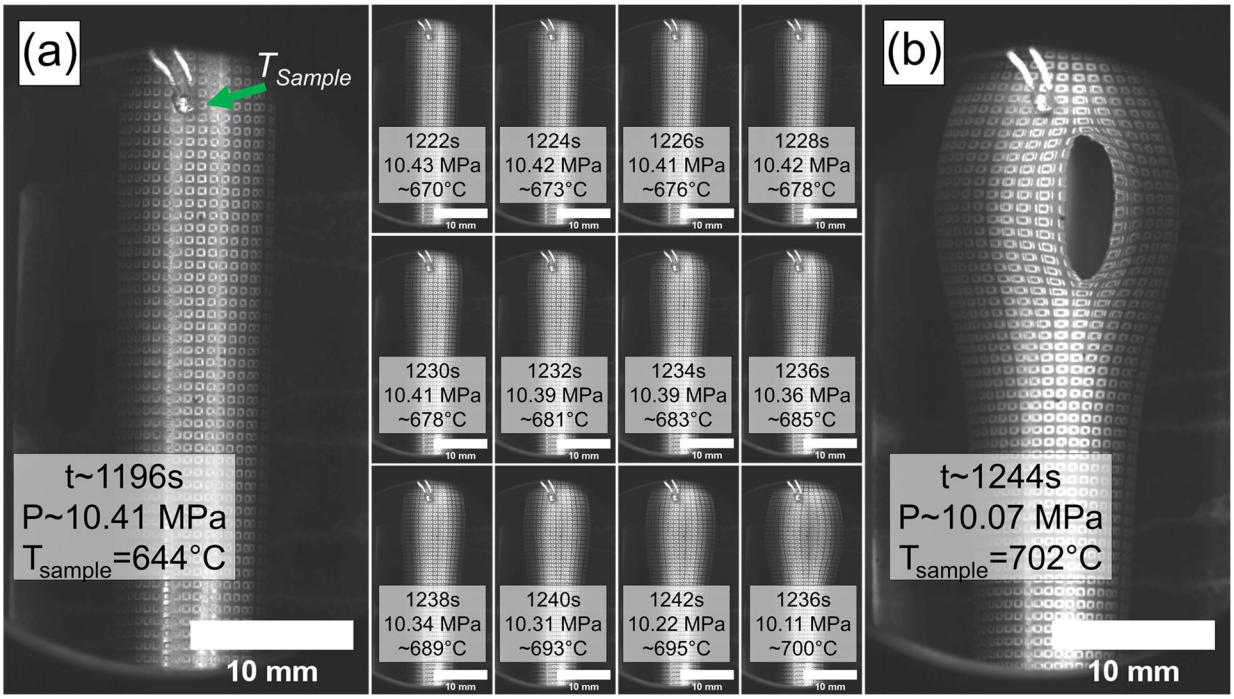

Figure 5-4 (a) Optical image of laser engraved Zr4 cladding prior to significant ballooning during 300° to 1200°C ramp at 1°C/s taken at 1196 s and series of images spaced ~2 seconds apart leading to (b) cladding burst ~48 s later.

An optical image and overlayed strain map is shown in Figure 5-5(a) immediately prior to burst. As anticipated, strain was dramatically increased closer to the burst region. An individual engraved square, labelled DIC object, was used to calculate hoop, axial, and radial strain over the entire 300° to 1200°C ramp until burst, with the temperature reading of T_{sample} taken as a temperature approximation, and is shown in a plot in Figure 5-5(b). Radial strain for these specimens cannot be measured directly by DIC, so it was calculated assuming conservation of volume.

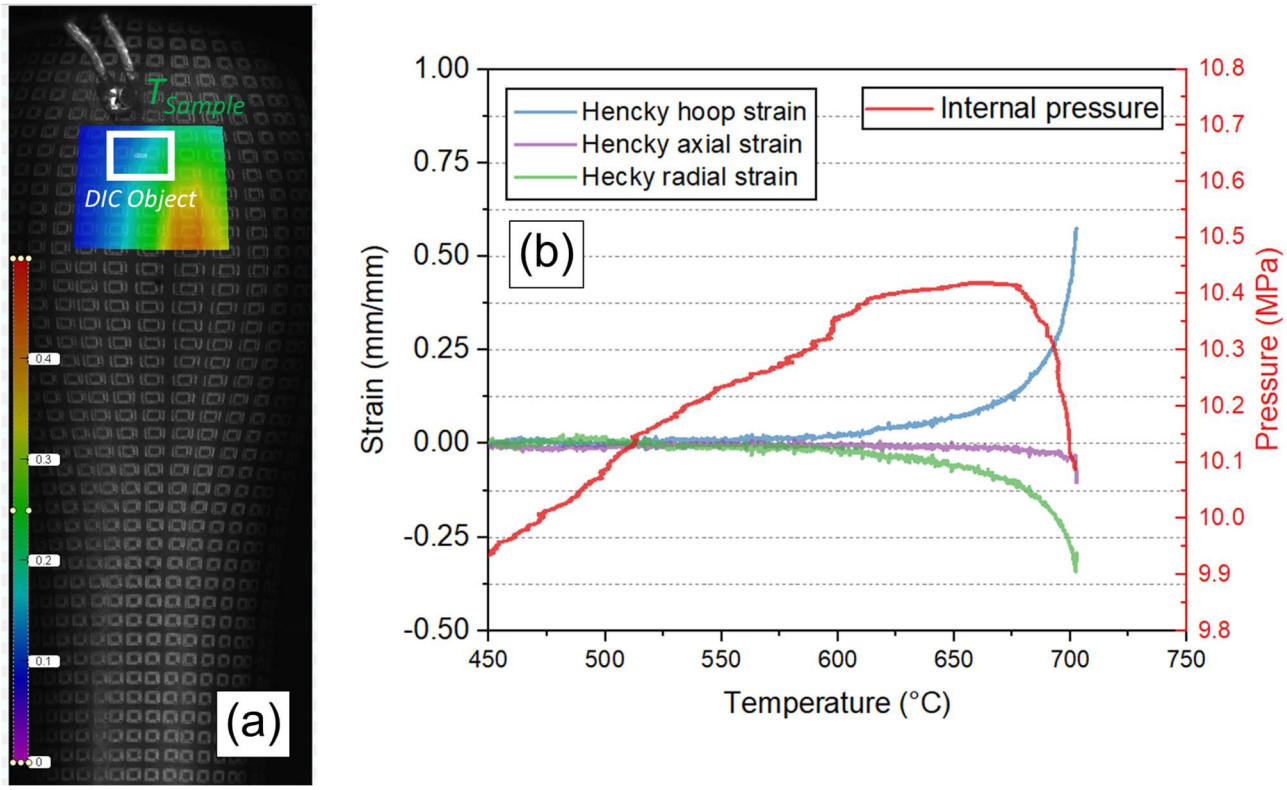

Figure 5-5 (a) Optical image showing colored strain map of hoop strain, immediately prior to burst. (b) Plot of the hoop, axial, and radial strain and internal pressure relationship with temperature, where hoop and axial strain was calculated over the entire 300° to 1200°C ramp (until burst) from the DIC object indicated in (a). Radial strain was calculated assuming conservation of volume based on the DIC-calculated hoop and axial strains, and its negative values suggest wall thinning, which is expected.

5.2.3 Correlation of DIC Strain with IR Imaging

Although there is a substantial loss of IR cladding resolution when the IR mirror is used, Figure 3-7(d), the IR thermal images provide insight about correlating DIC strain with observed temperature gradients. The optical image of the cladding immediately prior to burst and associated IR thermal image are shown in Figure 5-6(a) and Figure 5-6(b), respectively. A line scan of the thermal gradient down the cladding length is indicated by a white arrow in the IR image and blue arrow in the thermal profile in Figure 5-6(c). The line scan starts in the same region where the DIC object was located (the IR image is shifted downwards slightly due to the optical and IR camera sitting at different heights). Although burst temperature is taken as the T_{Sample} reading when de-pressurization occurs, the thermal profile indicates that the location where strain was calculated may be ~10°C lower. If strain were to be calculated in the exact region of burst, the actual temperatures may be closer to ~675°C. In lieu of accurate IR imaging, the temperature reading of T_{Sample} is taken as the burst temperature, keeping in mind that the actual region of burst may be at a lower temperature. During IR imaging of unpressurized Zr4 cladding during an identical thermal profile shown in Figure 5-1(a), the thermal gradient down the region where maximum deformation would occur was consistently ~40°C in the 600° to 800°C range, and could be roughly approximated as linear. Thus, if simultaneous optical and IR imaging without utilization of a mirror cannot be executed, thermal gradient could be estimated locally where strain is calculated.

The top compression fitting may have a profound impact on the burst behavior, Figure 3-6(b), as burst occurs in the top region of Zr4 cladding rather than the middle. This is potentially due to that region of the cladding reachest the highest temperatures, as the position of $T_{Control}$, which controls the programmed temperature ramping, likely experiences the highest temperatures of the entire cladding assembly. Future experimentation will be aimed to reliably ensuring burst occurs in the center of the Zr4 cladding length.

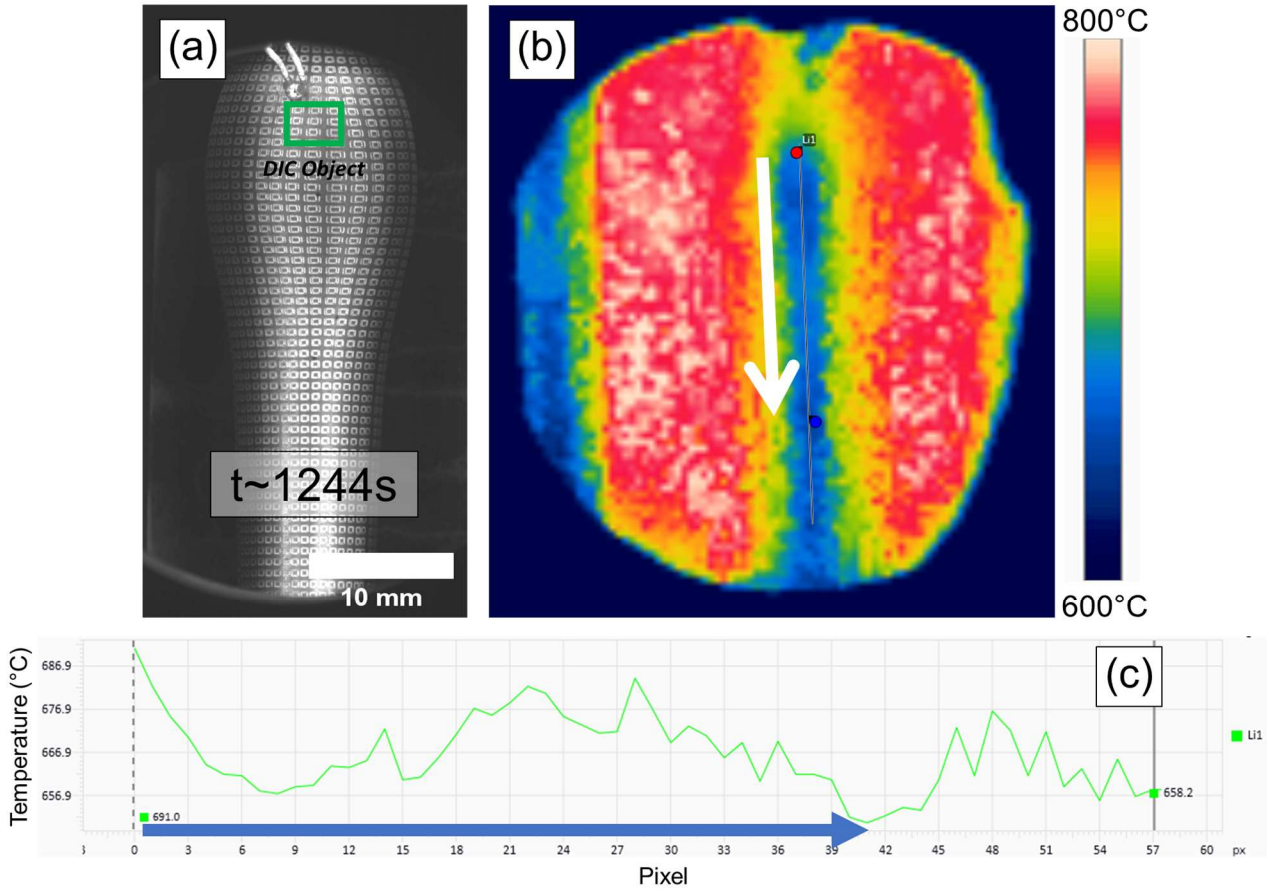

Figure 5-6 (a) Optical image of Zr4 cladding immediately prior to burst and (b) associated IR thermal image. (c) Line scan of thermal gradient down the cladding length, where direction and position are indicated by the white arrow in (b) and blue arrow in (c).

6. Summary and Conclusions

Out-of-cell burst testing at a nominal initial overpressure of ~ 8.2MPa with a 1°C/s heating rate was conducted on 76 mm lengths of unirradiated Zr4 cladding in air in an IR furnace with a viewing chamber bored through the side. A SiC "C" shell was incorporated into the cladding train assembly to eliminate IR reflections of the furnace lamps and to provide a more consistent optical illumination during testing. Laser

engraved patterns were used in conjunction with an optical camera and telecentric lens to quantify cladding deformation strain during burst testing with DIC, while an IR mirror, which split the visible and IR spectra, and a IR camera were used to quantify thermal gradients. Strain was successfully quantified up to and during burst with DIC, but there was significant loss of IR cladding resolution due to the IR mirror possessing poor reflectivity in the IR band relevant to LOCA temperatures. Although IR resolution is low, thermal gradients can be estimated and correlated with strain rates. Future work will investigate what impact patterning methods have on measured strains and burst behavior, implementing a new experimental set up to eliminate IR mirror utilization, and extension of the DIC/IR technique to a larger test matrix relevant to fuel code performance validation.

7. References

[1] F. J. Erbacher and S. Leistikow, “Zircaloy fuel cladding behavior in a loss-of-coolant accident: a review,” in *Zirconium in the Nuclear Industry*, ASTM International, 1987.

[2] NUREG, “FRAPTRAN: A Computer Code for the Transient Analysis of Oxide Fuel Rod,” 2001.

[3] V. Di Marcello, A. Schubert, J. van de Laar, and P. Van Uffelen, “The TRANSURANUS mechanical model for large strain analysis,” *Nucl. Eng. Des.*, vol. 276, pp. 19–29, 2014.

[4] K. Pettersson *et al.*, “Nuclear Fuel Behaviour in Loss-of-coolant Accident (LOCA) Conditions,” 2009.

[5] F. J. Erbacher, H. J. Neitzel, and K. Wiehr, “Cladding Deformation and Emergency Core Cooling of a Pressurized Water Reactor in a LOCA,” 1990.

[6] D. A. Powers and R. O. Meyer, “Cladding swelling and rupture models for LOCA analysis. Technical report,” Nuclear Regulatory Commission, 1980.

[7] W. Wiesenack, “Summary of the Halden Reactor Project LOCA test series IFA-650,” *IFE-OECD Halden React. Proj. HPR-380*, 2013.

[8] W. Wiesenack, “Summary and Comparison of LOCA Tests with BWR Fuel in the Halden Reactor Project Test Series IFA-650,” 2015.

[9] N. Capps *et al.*, “Integral LOCA fragmentation test on high-burnup fuel,” *Nucl. Eng. Des.*, vol. 367, p. 110811, 2020.

[10] C. P. Massey, K. A. Terrani, S. N. Dryepondt, and B. A. Pint, “Cladding burst behavior of Fe-based alloys under LOCA,” *J. Nucl. Mater.*, vol. 470, pp. 128–138, 2016.

[11] M. Snead, Y. Yan, M. Howell, J. Keiser, and K. Terrani, “Severe Accident Test Station Design Document,” *ORNL/TM-2015/556, Oak Ridge Natl. Lab.*, 2015.

[12] R. Nagy, M. Király, P. Petrik, and Z. Hózer, “Infrared observation of ballooning and burst of nuclear fuel cladding tubes,” *Nucl. Eng. Des.*, vol. 371, no. November 2020, 2020.

[13] P. M. Mathew and I. M. George, “Total Emissivity of Zircaloy-4 at High Temperatures,” *Proc. 17th Annu. CAN/CNS Conf, 1996*, vol. 1207, no. 8, pp. 2–5, 1996.

[14] R. W. L. Fong, M. Paine, and T. Nitheanandan, “ TOTAL HEMISPHERICAL EMISSIVITY OF PRE-OXIDIZED AND UN-OXIDIZED ZR-2.5N b PRESSURE-TUBE MATERIALS AT 600 °C TO 1000 °C UNDER VACUUM ,” *CNL Nucl. Rev.*, vol. 5, no. 1, pp. 85–93, 2016.

[15] E. V. Murphy and F. Havelock, “Emissivity of zirconium alloys in air in the temperature range 100-400°c,” *J. Nucl. Mater.*, vol. 60, no. 2, pp. 167–176, 1976.

[16] B. Bouvry *et al.*, "Multispectral pyrometry for surface temperature measurement of oxidized Zircaloy claddings," *Infrared Phys. Technol.*, vol. 83, pp. 78–87, 2017.

[17] J. Blaber, B. Adair, and A. Antoniou, "Ncorr: open-source 2D digital image correlation matlab software," *Exp. Mech.*, vol. 55, no. 6, pp. 1105–1122, 2015.

[18] B. Pan, W. Dafang, and X. Yong, "Incremental calculation for large deformation measurement using reliability-guided digital image correlation," *Opt. Lasers Eng.*, vol. 50, no. 4, pp. 586–592, 2012.

[19] M. N. Cinbiz, M. Gussev, K. Linton, and K. A. Terrani, "An advanced experimental design for modified burst testing of nuclear fuel cladding materials during transient loading," *Ann. Nucl. Energy*, vol. 127, pp. 30–38, 2019.

[20] H. Wang, D.-J. Jiang, L.-Y. Zhang, and B. Liu, "How to Realize Volume Conservation During Finite Plastic Deformation," *J. Appl. Mech.*, vol. 84, no. 11, 2017.

[21] K. A. Kane, S. K. Lee, S. B. Bell, N. R. Brown, and B. A. Pint, "Burst behavior of nuclear grade FeCrAl and Zircaloy-2 fuel cladding under simulated cyclic dryout conditions," *J. Nucl. Mater.*, vol. 539, p. 152256, 2020.

[22] R. H. Chapman, *Multirod burst test program*, vol. 88. Department of Energy,[Office of Energy Technology], Oak Ridge National …, 1978.